Journal of Colloid and Interface Science 649 (2023) 302–312

Contents lists available at ScienceDirect

Journal of Colloid And Interface Science

journal homepage: www.elsevier.com/locate/jcis

Spatio-temporal programming of lyotropic phase transition in nanoporous microfluidic confinements

Vamseekrishna Ulaganathan, Anupam Sengupta *

Physics of Living Matter Group, Department of Physics and Materials Science, University of Luxembourg, 162 A, Avenue de la Faïencerie, L-1511 Luxembourg City, Luxembourg

GRAPHICAL ABSTRACT

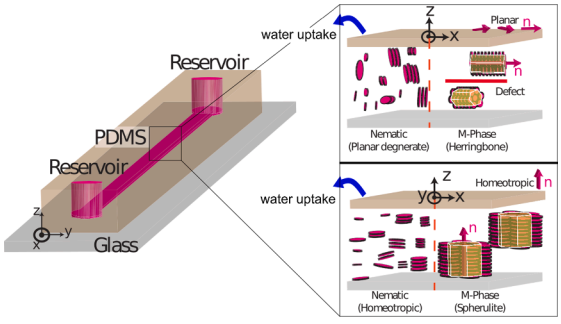

Programmable lyotropic phase transition driven by nanoporous surfaces

ARTICLE INFO

Keywords:
Nanoporosity
Lyotropic chromonic liquid crystals
PDMS
Microfluidics
Wettability
Phase transition
Surface anchoring
Topography

ABSTRACT

Hypothesis: The nanoporous polydimethylsiloxane (PDMS) surfaces of a rectangular microfluidic channel, selectively uptakes water molecules, concentrating the solute molecules in an aqueous phase, that could drive phase transitions. Factors such as surface wettability, channel geometry, the surface-to-volume ratio, and surface topography of the confinements could play a key role in tuning the phase transitions spatio-temporally.

Experiments: Using a lyotropic chromonic liquid crystal as model biological material, confined within nanoporous microfluidic environments, we study molecular assembly driven by nanoporous substrates. By combining timelapse polarized imaging, quantitative image processing, and a simple mathematical model, we analyze the phase transitions and construct a master diagram capturing the role of surface wettability, channel geometry and embedded topography on programmable lyotropic phase transitions.

Findings: Intrinsic PDMS nanoporosity and confinement cross-section, together with the imposed wettability regulate the rate of the *N*-M phase transition; whereas the microfluidic geometry and embedded topography enable phase transition at targeted locations. We harness the emergent long-range order during *N*-M transition to actuate elasto-advective transport of embedded micro-cargo, demonstrating particle manipulation concepts governed by tunable phase transitions. Our results present a programmable physical route to material assembly in microfluidic environment, and offer a new paradigm for assembling genetic components, biological cargo, and minimal synthetic cells.

* Corresponding author.
E-mail address: anupam.sengupta@uni.lu (A. Sengupta).

https://doi.org/10.1016/j.jcis.2023.06.010
Received 15 November 2022; Received in revised form 4 May 2023; Accepted 3 June 2023
Available online 5 June 2023

1. Introduction

Microfluidics enabled miniaturizing technologies such as chromatography, chemical reactions, and mixing systems by using "soft" elastomers like polydimethylsiloxane (PDMS) in fabrication [1]. PDMS is mixed with a cross-linker to form a rubber-like material, which is cast onto silicon wafers with micron-sized channel designs, then bonded to glass substrates that can be viewed under a microscope (Fig. 1a). The possibility of integrating topographical features [2], deformable walls [3], modular elements allowing tunable fields and gradients [4], and nanoporous elements [5] has enabled precise control and manipulation of multi-scale transport processes relevant for a wide range of applications in physical, chemical and biological settings.

PDMS is an inherently hydrophobic material that has a nanoporous ultrastructure [6]. Surface treatments including UV-ozone, and air or oxygen plasma exposure render PDMS hydrophilic [7–9], however with a steady hydrophobic recovery under normal environmental conditions [8,9]. Plasma treatment oxidizes PDMS surface adding three to four oxygen atoms to a silicon atom [10], making it hydrophilic (Fig. 1b). Dimethyloctadecyl[3-(trimethoxysilyl)propyl] ammonium chloride (DMOAP), a well-known silane used for incorporating homeotropic (normal) molecular anchoring of liquid crystal molecules [11–13], induces hydrophobicity on both PDMS and glass surfaces. When LCs are introduced in the channel, the molecules align either parallel (perpendicular) to the plasma (DMOAP) treated surfaces [9].

The intrinsic material anisotropy of liquid crystals (LCs) makes them complex fluids with diverse functional properties [12,14,15], including hydrodynamic attributes. Harnessing the anisotropic coupling between flow and molecular ordering of thermotropic LCs offers a new approach to conventional microfluidic concepts based on isotropic fluids [16,17]. LC-based microfluidics can enhance transport in bulk [18,19], and tailor topological defects as self-assembled rails for micro-cargo transport [20]. Flow-driven orientational changes, visco-elastic effects under microscale confinements, and surface anchoring enable tunable flow profiles and surface-controlled hydrodynamic resistance [21,22]. Lyotropic LCs, formed by the anisotropic assembly of water-soluble disc-shaped molecules, are biologically relevant and exhibit LC structures due to their ability to undergo reversible changes in morphology and thermodynamic phase [24]. Examples of lyotropic LCs include amphiphilic lipids found in cellular membranes, deoxyribonucleic acid (DNA) in chromosomes, and cytoskeletal and muscle proteins [23]. Lyotropic chromonic liquid crystals (LCLCs) are a special class of lyotropic LCs that form linear aggregates held together by non-covalent interactions, leading to self-assembled nematic (N) phase or columnar (M−phase) with a hexagonal arrangement [25,26]. Common LCLC examples include sunset yellow (SSY), an azo dye used as a food additive, and disodium cromoglycate (DSCG), an anti-asthmatic drug, used in the current study. While the nematic phase consists of short columnar stacks which appear at room temperature for low LCLC concentrations, the columnar phase emerges at high concentrations wherein the stacks self-assemble into two-dimensional hexagonal array of extended columns in the M−phase [27]. In both the N- phase and the M−phase, the director is average orientation of columnar axis of the stacks [28,29], with the latter manifesting as archetypal herringbone or spherulite textures [30]. Unlike thermotropic LC phases which are sensitive only to changes in the temperature, LCLC materials may undergo phase transitions even under constant temperature due to changes in the concentration.

LCLC confined within nanoporous microfluidic devices, as in our PDMS-based microchannels, may undergo isothermal phase transition under appropriate conditions [30]. The presence of nanopores in PDMS

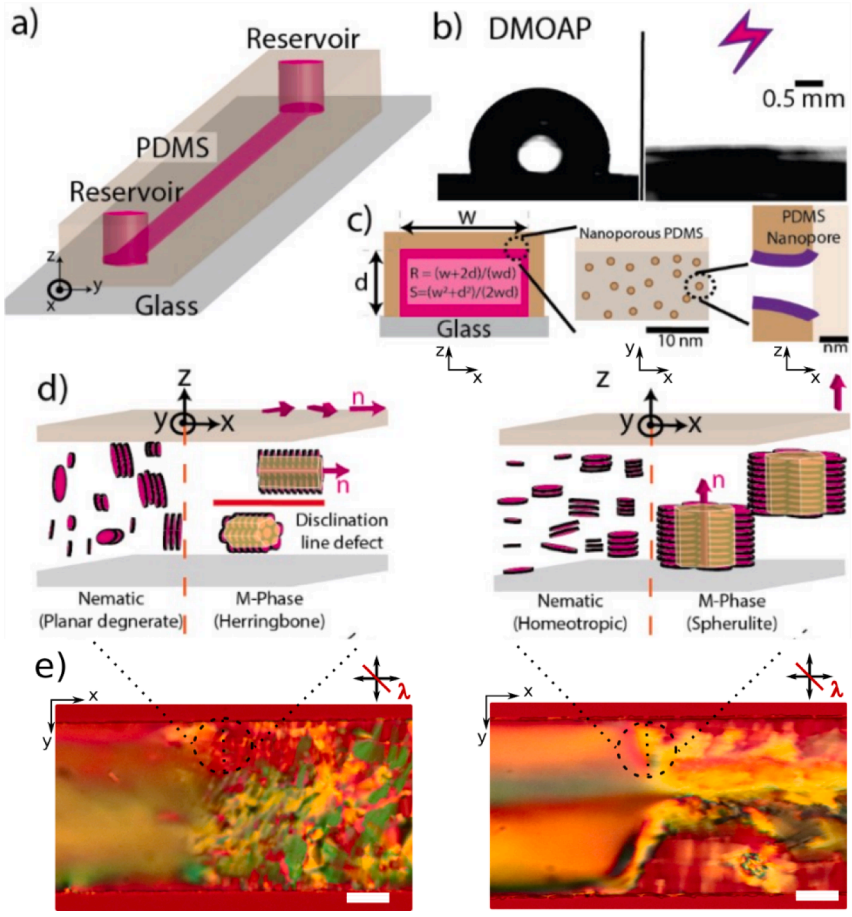

Fig. 1. (Colour figure) Nanoporous microfluidic confinements induce lyotropic phase transition. (a) Schematic representation of a glass-PDMS microfluidic channel with both openings acting as reservoirs at the initial LCLC concentrations. The channel depth was kept constant ($d \approx 10$ μm), whereas the width and overall channel geometry were varied in our experiments. **(b)** The wettability of PDMS walls was varied by appropriate surface treatments: coating with the silane DMOAP rendered the surfaces hydrophobic, contact angle of water ≈ 106.90 ± 2.95° (n = 14); while exposure to air plasma turned the surfaces hydrophilic, contact angle ≈ 0°. The contact angle of water on untreated PDMS surface was found to be 100.60 ± 0.27° (n = 10). **(c)** Varying the aspect ratio of the channels (A = width /depth = w/d) alters the surface-to-volume ratio (R) and the shape factor (S) of the microfluidic confinements, defined respectively as $R = (w + 2d)/wd$, and $S = (w^2 + d^2)/2wd$. PDMS nanopores, indicated as darker circles, retain the native hydrophobicity even after the DMOAP and plasma surface treatments, thus generating a relative difference in the wettability that drives the transport and selective uptake of water molecules from the LCLC phase. The axes of cross-sections are presented below the schematic representations. **(d)** Molecular ordering of the LCLC corresponding to the nematic and columnar phases, as observed by polarized optical microscopy (POM) with 530 nm retardation λ-plate The N-M transition front is clearly distinguished by the difference in the texture on either side: nematic and M−phase within plasma treated channels (left panel), and within DMOAP-treated microchannels (right panel); **n** denotes the local director. The vertical dashed lines in **(d)** and **(e)** indicate the regions of transition from nematic to (left image) herringbone and (right image) spherulites texture. Scale bar: 50 μm.

drives selective absorption of water molecules (Fig. 1c), thus enhancing the concentration and shifting the thermodynamic phase of the DSCG. Yet, how confinement dimensions, and surface properties control the initiation and rate of LCLC phase transitions remain unknown. Here, we leverage PDMS-based microfluidics to confine DSCG, and control the phase transitions from disc-shaped mesogens (isotropic) to aligned cylindrical stacks (nematic), and finally into the honeycomb structures of the M−phase. By systematically varying the surface wettability (and anchoring), confinement cross-section and shape, and the channel topography, we program phase transitions at will under isothermal conditions, within generic microfluidic geometries. The presence of ports on the either ends of the microfluidic device acts as reservoir, allowing material transport to the center of the channel [36], thus concentrating the DSCG solution at the center of the channel. Though concentration-dependent phase transitions of LCLCs have been studied in the past few decades [33–35], how this process can be controlled spatially and temporally remains unexplored. We thus confine the LCLCs within a nanoporous confinement, thus triggering a selective uptake water molecules, ultimately inducing the LCLC phase transition. Supported by a simple mathematical model, our results uncover spatio-temporal evolution of self-assembled LCLC structures, offering a surface-controlled physical pathway for molecular assembly and cargo transport, with potentially far-reaching ramifications on our current understanding of the prebiotic evolution mediated by nanoporous clay materials like montmorillonite [31].

2. Materials and methods

We use soft lithography to design the microfluidic devices, and quantify the isotropic-to-nematic-to-columnar phase transitions using polarization optical microscopy. Overall, DMOAP-treated surfaces yield homeotropic anchoring and low surface wettability, and plasma-treatment generated planar anchoring and high surface wettability [9,30]. The intrinsic nanopores of PDMS remain unaffected due to these surface treatments [32]. The dynamics of the nematic-columnar phase transition are captured using timelapse imaging mode under fixed temperature conditions. The time of the appearance of the M−phase – detected by the moving *N*-M interface – shows a strong dependence on the channel geometry (width and depth) and surface anchoring (degenerate planar vs. homeotropic). The time taken for the entire region of observation to undergo phase transition ($t_{completion}$) was noted for each case, alongside measurement of the *N*-M front propagation speed. The experiments reported here were repeated a minimum of 3 times to determine the statistics, and to ensure the reproducibility of our results. Table 1 lists the parameters, units and the symbols used in this work.

2.1. Materials and solution preparation

We prepared the lyotropic chromonic liquid crystal solutions using DSCG in deionized millipore water, vortexed for 30 min and stirred at room temperature for 12 h to obtain a homogeneous solution. The silane, Disodium cromoglycate and dimethyloctadecyl [3-(trimethoxysilyl) propyl] ammonium chloride solution (DMOAP) was purchased from Sigma-Aldrich. 4-cyano-4-pentyl-1 and used as received. All the solvents used were of GC purity (≥99.8 %) and sourced from Carl-Roth.

2.2. Microfluidic confinement

We prepared the PDMS-glass microfluidic devices using the fabrication protocols outlined previously [23]. Our microfluidic chips comprised 3 walls of polydimethylsiloxane (PDMS, Sylgard 184, Dow Corning) reliefs, prepared by following the standard soft lithography techniques. The PDMS reliefs were bonded to glass substrates via air plasma exposure. Before bonding, the glass substrates were thoroughly cleaned with isopropanol and dried on a hot plate (80 °C for approximately 30 min). Microchannels with rectangular cross-sections having different geometries are considered in this work: linear, *T*-shaped, septapod (seven-armed), and channels with topographical features (single or regular array of pillars). For the linear channels, the depth (d) kept was kept at 10 μm, while three different channel widths (w) were investigated: 75 μm, 200 μm, and 345 μm. The distance between the inlet and the outlet port was typically set to 20 mm, defining the length (l) of the channel. Cylindrical holes (1.5 mm diameter) at the ends of the channels provided the housing for microfluidic tubings, which also served as the reservoirs.

2.3. Filling the microfluidic channels filled with lyotropic LC

The experimental protocols are based on our previous publication [30]. Solutions with 12 or 14 wt% of DSCG solution was gradually filled in microfluidic channels using a syringe pump by placing the glass side on a hot plate at 45° C to make sure the solution is in an isotropic state, thus preventing flow-induced surface alignment. The open ends of the Teflon tubings, fixed on both ends (ports) of the channel, were sealed with playdough to ensure no evaporative losses during the long-term timelapse image acquisition. Before starting the experiments, the midpoint of the channel was marked on the glass side (using a marker), and used as a reference region of interest for the POM. All measurements were carried out around the central region of the channel, close to the geometric midpoint, allowing us to capture the initiation of the nematic to M−phase transition.

2.4. Surface anchoring and boundary conditions

Microfluidic devices were functionalized for contrasting wettability and surface anchoring conditions: air plasma exposure yielded high wettability (low contact angle) and degenerate planar anchoring condition; whereas DMOAP treatment resulted in low wettability (high contact angle) and homeotropic surface anchoring. Since the effect of plasma treatment degrades under normal environmental conditions [9], freshly treated channels were immediately filled with the LCLC. To induce homeotropic alignment, the channels were first filled with 0.4 wt % aqueous solution of DMOAP, and then thermally cured at 80 °C for 2 h, rendering both the PDMS and glass surfaces hydrophobic with homeotropic boundary conditions. Detailed steps of the plasma exposure and DMOAP treatment can be found in refs [12]. The surface wettability and anchoring conditions obtained using the above treatments were respectively validated using de-ionized water and thermotropic nematic LC, 4-cyano-4-pentyl-1, 10-biphenyl (5CB, procured from Synthon Chemicals and used as received) as outlined in our previous studies [13].

2.5. Polarization optical microscopy and image acquisition

The LCLC director orientation, phase transition, and the elasto-advective transport of microscale particles in the PDMS-glass microfluidic chips were studied using a polarized light microscope (Eclipse LV100N-POL, Nikon), equipped with different objectives ×5, ×10, ×20, and ×40 objectives. The sample temperature was maintained with a Linkam (PE120) heating/cooling stage. Experiments were conducted under different orientations of the crossed-polarizers using transmitted white light: (a) the microfluidic channel parallel to one of the crossed-polarizers, (b) the channels oriented at 45° with respect to the polarizers, and (c) with and without the insertion of a 530 nm phase-retardation plate. POM images (6000 × 4000 resolution), and full HD coloured videos (1920 × 1080 resolution) recorded at a frame rate of 25 frames per second were acquired using a digital Canon EOS77D camera. The acquired POM data were quantified using a combination of ImageJ, VideoMach, and MATLAB softwares [13,21].

2.6. Bulk water uptake by PDMS molds

The intrinsic nanoporous structure of PDMS allows it to uptake liquids depending on their polarity, including liquid crystals and water [9,36]. In this work, the rate of water uptake by bulk PDMS was obtained by measuring the difference in weight of PDMS molds before and after immersing them in a bath of de-ionized water. PDMS molds of dimension 40 mm × 20 mm × 6 mm were cut from larger chunks, cleaned with ethanol in an ultrasound bath, and dried on a hot plate before recording the dry weight of the PDMS molds. The dry weight of the molds was measured using a sensitive balance (XSR204DR, Mettler Toledo, BENELUX) with a precision of 100 μg, right after the molds were treated using DMOAP and air plasma following the protocols mentioned above. Thereafter the molds were immersed fully in water baths maintained at a fixed temperature. Similar experiments were carried out using untreated PDMS molds, providing control measurements. The immersed molds were weighed periodically to determine the change in the weight due to the uptake of water. Similar experiments were conducted for three different temperatures to obtain the pseudo-second-order kinetics. Details of the data fitting can be found in the supplementary section.

2.7. Contact angle measurements

The contact angle of the water (de-ionized Millipore) on the surface-treated substrates was measured using a standard goniometer (Dataphysics, OCA 15-EC, Filderstadt, Germany) in static mode via sessile drop technique, with a precision of ±0.1°. A small but defined volume (tens of microliters) of water was dispensed on the treated substrate, which was then imaged to identify the base line (liquid–solid interface) and the contour of the water drop (liquid–air interface). The contact angle was obtained by fitting the contour line with appropriate equation provided by the goniometer software, SCA 20.

3. Results and discussion

3.1. Surface wettability and channel confinement affecting the phase transition

DSCG molecules in an aqueous solution exist as disc-shaped mesogens in the isotropic state which stacks to form cylindrical aggregates forming a nematic state [25]. With further increase in concentration – driven either by lowering temperature or water content – the cylindrical rod-shaped colloidal aggregates assemble into a hexagonal honeycomb structure forming M−phase, while the alignment of these aggregates are still determined by the surface they interact with (Fig. 1d). Such change in phase can occur within microfluidic channels when water is taken up by PDMS, resulting in the formation of distinct anchoring-specific textures when the M−phase emerges (Fig. 1e). It must be noted that cylindrical ports (ϕ: 1.5 mm, h: ∼6mm) at the either ends of the channels have much larger volumes than the volume of the DSCG confined within the microfluidic chips (l: ∼10 mm, w: 50 to 350 μm, d: 10 to 25 μm). As the three PDMS-walls selectively absorb water molecules, the volume of water lost from the DSCG solution in the channel is compensated by the relatively higher water content present in the DSCG solution located at the ports which serve as reservoirs of DSCG in nematic phase (or isotropic phase, depending on the initial concentration of the experiment). By symmetry arguments, it can be thus shown that molecular influx of water from the ports converges at the midpoint of linear microchannels [36], resulting in a local maximum of the DSCG concentration near the channel center. This was confirmed in our experiments, and consequently the channel central region was identified as the zone of observation for all measurements.

Once the nematic to M−phase transition initiates at the center of the microchannel, a distinct nematic-M−phase front propagates along either direction, ultimately filling the entire channel length with M−phase. Fig. 1e shows a snapshot of the propagating *N*-M−phase interface. Similarly, when we start our experiments using DSCG in isotropic phase, first the nematic phase appears, followed by the M−phase. Now, we will focus on the appearance of the M−phase texture under distinct anchoring conditions from an initial nematic phase.

3.2. Surface anchoring and confinement synergistically regulate columnar textures

The grain structures formed by the M−phase is presented in Fig. 2. The effect of the surface treatment could be clearly distinguished by quantifying the grain widths for the plasma and DMOAP treated channels. We employ digital image processing techniques to arrive at the texture parameters: first we image the freshly formed M−phase textures between two different cross-polarizer orientations (at 0° and 45° relative to the channel length), and then extract pixel-by-pixel difference in the polarized signals to arrive at the grain width presented in Fig. 2a, b. This analysis is conducted across entire width of the channels, to finally obtain the variation of the grain widths in the transverse direction (Fig. 2c and d). Further details on the image analysis algorithm can be found in the Supplementary materials (section S1). While homeotropically aligned self-assembled hexagonal structures yielded larger projected grain width, the planar anchored surfaces supported grain widths with lower mean width (Fig. 2c and d), in agreement with existing literature [37]. We further observe that, for a given surface anchoring condition, the grain width increases consistently as one moves from the confining walls toward the long symmetry axis of the microchannel, bearing a qualitative similarity with solidification of liquid metals cast in molds. In freshly formed solid metal phase, grain widths are smaller closer to the surface (known as the chill zone), which then gradually increase as the distance from the surface increases [38]. Analogous to the rate of water uptake by PDMS surfaces (*i.e.*, mass transport), it is the rate of cooling associated with liquid–solid metal systems that determines the grain dimensions and their coherence [39–41]. The dependence of the grain textures on the rate of the heat transport allows us to hypothesize that the *N*-M−phase transition can be equivalently tuned by regulating the uptake of water by the PDMS surfaces.

In the case of DSCG solution, the transition from the nematic to the M−phase is analogous to liquid–solid metal solidification process, as the fluid-like nematic phase transforms to a solid-like M−phase. As the diffusion of heat during cooling in metal casting promotes the phase transition, in our case the selective diffusion of water molecules into the nanoporous PDMS matrix drives the local enhancement of DSCG concentration, ultimately initiating the *N*-M phase transition. The effect of anchoring conditions on M−phase formation is clearly captured in Fig. 2: on average, the characteristic grain width under homeotropic anchoring conditions is twice larger (Fig. 2c) than the grain width observed in channels with degenerate planar anchoring conditions (in the middle of the plasma-treated channels, the size ranges from 4 μm to 8 μm, Fig. 2d). This trend is reversed when we quantify the total number of grains within the same normalized bins (Supplementary, Figure S1): the density, *i.e.*, number of grains in a given area, maximizes in the vicinity of the channel walls, decreasing gradually toward the central region of the channel. Overall, the number of grains in homeotropic conditions is lower than that in planar conditions. Interestingly, the variation of the number of grains over the grain width corresponding over any region falls onto a master curve $y = ax^b$, where y and $\times$ represent the number of grains and size respectively, with $a = 1101.85$ and $b = -0.97$ (Fig. 2e). The corresponding insets present the trend for DMOAP- (top) and plasma- (bottom) treated channels: within DMOAP-treated, the grain width and number vary widely with respect to the channel dimensions; whereas within plasma-treated channels, the impact of channel dimensions is less pronounced. In summary, the effects of anchoring and confinement dimensions set a trade-off, such that the anchoring–dependent difference in the relative grain width and numbers get compensated as channel widths are reduced. This is seen

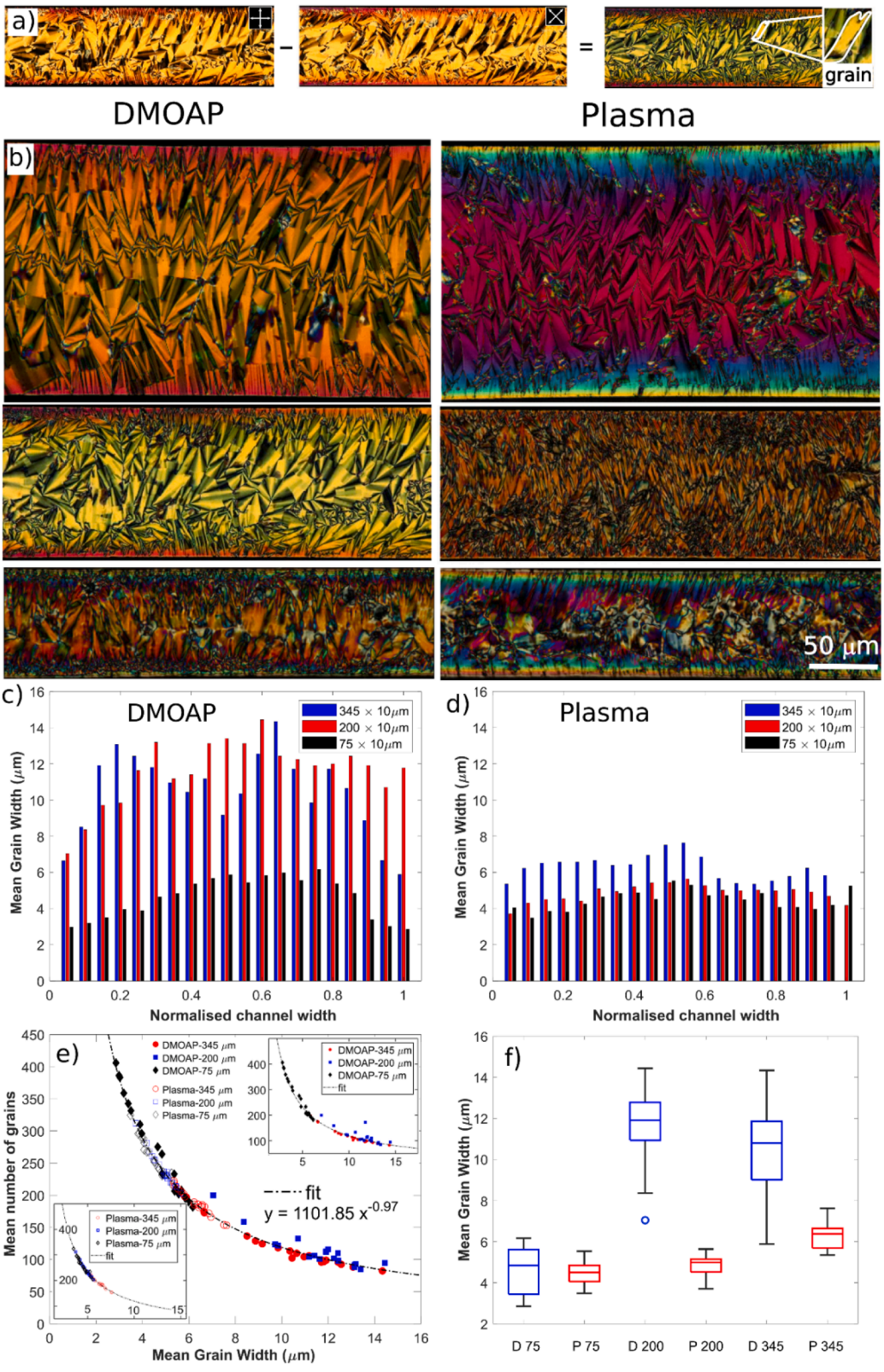

Fig. 2. (Colour figure) Columnar (M) phase textures are governed by the microfluidic confinement and surface anchoring. (a) The M−phase grain boundaries are clearly visualized after quantitative image processing (see section S1 in supplementary), whereby polarized optical micrographs are obtained for different orientations of crossed-polarizers (at 0 and 45°to the channel length) of a given region. The absolute difference of the polarized light signals reveals the grain width of the columnar phase. In contrast, the smooth nematic textures do not show any grainy feature. (b) Quantitative image processing reveals M−phase textures for the DMOAP- (left column) and plasma- (right column) treated confinements. The channel dimensions span (w × d): 350 μm × 10 μm, 200 × 10 μm and 75 × 10 μm from top to bottom in both columns. (c) Overall, the mean grain width is larger for DMOAP-treated channels compared to the plasma-treated confinements (d), due to the relative difference in the projected areas of the spherulite (homeotropic) and herringbone (planar) textures, as shown in Fig. 1d. For a given surface-treatment, the grain width scaled with the channel width, with the largest grains observed in the vicinity of the channel center line (at normalized width ~0.5). Wider channels yield larger grains and vice versa; the corresponding number of grains distributions are provided as supplementary data. (e) The markers represent DMOAP (closed symbols) and Plasma treated channels (open symbols) and each shape represents different widths (w) of the channel for depth d = 10 μm. Number of grains and grain width data obtained from microchannels with different surface anchoring conditions and aspect ratios fall on a master curve, $y = ax^b$ where y and × represent the number of grains and size respectively, with a = 1101.85 and b = -0.97. Insets present the distribution of the data points on the master curve for the DMOAP- (top) and plasma- (bottom) treated channels. (f) Box plots capture the variation of the mean grain width across the cases discussed above.

clearly in the case of $w = 75$ μm, the mean grain width is statistically comparable under both anchoring conditions (Fig. 2f). The aspect ratio of the freshly formed M−phase grains is longer in plasma-treated channels, compared to those formed under DMOAP-treated confinements, manifesting typically as the herringbone and spherulite textures respectively. Since the long axis of the hexagonal assembly of cylindrical stacks of DSCG (see Fig. 1d) is aligned parallel to the channel inner surfaces, the corresponding grains – comprising several hexagonal assemblies packed together – develop with a higher aspect ratio. In the case of homeotropic anchoring, the circular projection of the cylindrical stacks aligns parallel to the surface (*i.e.*, the long axis is perpendicular to the channel surface), thus resulting in relatively larger grain widths. The

decrease in the grain width observed with the reduction of the channel width could be reasoned due to the faster diffusion of water under the larger surface-to-volume ratio, $R = (w + 2d)/wd$, where w and d respectively indicate the width and depth of the microchannels.

3.3. Surface wettability and microfluidic shape factor govern the rate of phase transition

Building up on Chvorinov's relation for the solidification time in metal casting, given by $t = \beta(\frac{V}{\alpha})^{\eta}$, where V, α, η are the mold volume, surface area, and a constant; and β is the mold constant, a function of the material properties including density and heat capacity [42], we propose that the time required for the nematic to the M−phase transition should be inversely proportional to R, the surface-to-volume ratio of the channel. The basic theory behind the metal solidification process has been reasonably well established and it is a phase transition occurring in a single component system. In our study, the phase transition of DSCG is a two-component system where water and DSCG molecules exists and the phase change occurs when DSCG/water ratio changes, due to water absorption by PDMS. Such phase transition due to concentration change in LCLC systems via water evaporation has been studied by several authors [43–45]. Therefore, it is important to understand the water absorption kinetics by PDMS which eventually triggers the phase transition of nematic to the M−phase. To understand the water absorption kinetics by PDMS, we record the increase in the weight of PDMS rectangular molds (similar size, different anchoring conditions) immersed in bath of de-ionized water, relative to corresponding dry weights. The percentage change (PC) of the weight of the PDMS molds pre-treated with plasma and DMOAP, shows a striking difference (Fig. 3a and b). While hydrophilic surfaces are known to better absorb water molecules than hydrophobic surfaces [46], here we report an opposite trend: the water absorption capacity (equilibrium PC%), and the corresponding rate of

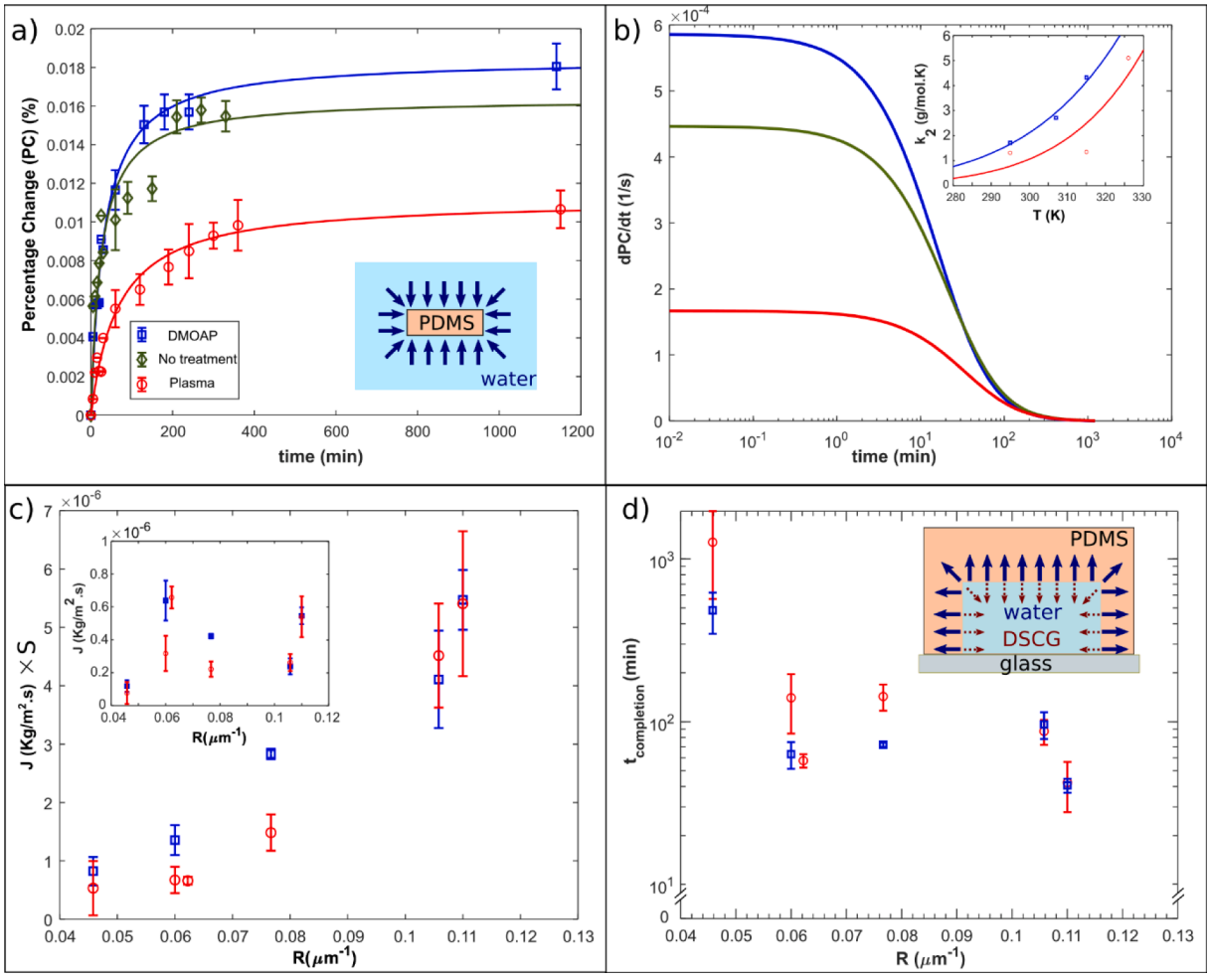

Fig. 3. (Colour figure) Surface wettability and confinement cross-section govern the rate of isothermal N-M phase transition. (a) Percentage change (PC, in %) in the weight of surface-treated PDMS blocks submersed in water, shown as (blue □) and (red ○) for DMOAP- and plasma-treated surfaces respectively, while the native PDMS surface is indicated by (black ◊). DMOAP enhances PDMS hydrophobicity, while plasma treatment enhances surface hydrophilicity: this leads to a relative reduction (for DMOAP) and enhancement (for plasma) of wettability relative to the native PDMS-nanopore wettability. Solid lines in respective colors fit the experimental data using pseudo-second order kinetics. The experiments were done at room temperature (23 ± 1 °C). The inset shows the schematic of water being absorbed by the rectangular PDMS blocks. (b) The gradient dPC/dt is obtained from the pseudo second order fit as shown in (a) that is plotted against time (also at 23 ± 1 °C). The inset plots the rate constant k_2 for PC values obtained at three different experimental temperatures: T ≈ 23 °C, 34 °C, and 42 °C for DMOAP-treated samples; T ≈ 23 °C, 42 °C, and 53 °C for the plasma-treated samples. The data is fitted to the Arrhenius equation, further information on the fitting is available in the supplementary section. Blue and red lines indicate the DMOAP- and plasma-treated cases respectively. (c) The water uptake rate per unit surface area (J) is regulated by the cross-sectional shape of the PDMS-glass microchannels: J × S shows a monotonic increase with the corresponding surface-to-volume ratio (R). Here S is the shape factor as defined in Fig. 1c. The inset shows the variation of J with the surface-to-volume ratio, R. (d) The time taken for the M−phase to cover a given region of observation (initially nematic phase) reduces with the surface-to-volume ratio, for both the wettability conditions. The inset shows a schematic of the PDMS-glass microchannel cross-section, the water uptake proceeds through the three bounding PDMS surfaces thus leading to an increase of local DSCG concentration at the PDMS surfaces.

absorption by the plasma-treated PDMS molds were low compared to the DMOAP-treated molds of similar dimensions. The plasma treated PDMS surfaces are known to form thin barrier films of SiO_x due to reaction of O_2 with the silicone, preventing diffusion of molecules through pores [47]. As control, the untreated PDMS molds (which are inherently hydrophobic) exhibited better water absorption property (both uptake rate and saturation *PC*) than the plasma-treated molds, however weaker when compared to DMOAP-treated counterparts. Our results indicate that the plasma treated PDMS surface hinders transport of water molecules through the nanopores (as shown in Fig. 3 b), due to the generation of a wettability gradient and possible formation of barrier film between the continuous surface (rendered hydrophilic due to plasma-treatment) and the nanopores which retain their intrinsic hydrophobicity. Such a gradient of wettability can cause water molecules to remain strongly associated with the continuous PDMS surface, rather than diffusing into the nanopores [48]. However, the trend reverses when the continuous surface has lower wettability (induced by the DMOAP-treatment), relative to the nanopores. In this case, the water molecules are preferentially driven into the nanopores, thus enhancing the overall water uptake rates.

Different surface-treatments impact not only the anchoring of the DSCG molecules, but in addition, control the phase transition time. To validate the suggested mechanism, we varied the temperature of the water bath where the PDMS molds were immersed. Since the surface interaction energy between the pre-treated PDMS surface and water molecules is altered, impeding (or promoting in the case of DMOAP treatment) the diffusion of water molecules into the nanoporous matrix should depend on the thermal energy. Higher thermal energy should enhance the uptake kinetics irrespective of the anchoring effects. This is confirmed in Fig. 3b inset, which presents the variation of the experimental rate constant k_2, as a function of the bath temperature. The data were fitted using a pseudo-second-order kinetics reaction, and the fitted lines represent the Arrhenius equation $k_2 = A_0 e^{-\frac{E_a}{RT}}$ where A_0 is a constant and E_a is the activation energy. More details on data fitting to pseudo-second-order kinetic could be found in the section S3 in the supplementary. For the current set of data, the activation energy offers a quantitative measure of the energy barrier that the water molecules need to overcome, which is higher for the plasma-treated surface ($E_{a,\ planar} \sim 4.48 \times 10^4$ J/mol) than that of the DMOAP-treated surfaces ($E_{a,\ homeo} \sim 3.54 \times 10^4$ J/mol).

Fig. 3c presents the flux, J, of water uptake by the PDMS per unit time and surface area, considering the three PDMS walls of the rectangular channel. J is estimated by the time it takes to complete the phase transition over a given region of observation (Fig. 3d), once the channel has been filled with 14 % DSCG solution (nematic phase). As discussed earlier, we fix the observation point close to the middle of the channel length, allowing the water molecules absorbed by the PDMS to be replenished by the water molecules from the DSCG reservoirs in the nematic phase at the channel ports. Section S2 in the supplementary presents how the water uptake rate is estimated from *N*-M phase transition time in the observation frame. Confirming previous tracer experiments by Randall *et al.* [36], we provided a physical framework for the *N*-M phase transition in LCLCs confined within nanoporous microfluidic settings. We infer that the local DSCG concentrations will increase in the middle of the channel, marking the initiation of the *N*-M phase transition. The inset plots the variation of J as a function of the surface-to-volume ratio, R, for both the plasma- and the DMOAP-treated channels. The J vs R plots fail to capture a clear trend and indicate that for relatively close values of R (0.06 μm^{-1} and 0.062 μm^{-1}), values of J can be significantly different. This seeming discrepancy could be resolved by accounting for the shape of the microfluidic channels, in addition to their surface-to-volume ratios. Empirically, we extracted the shape factor, $S = (w^2 + d^2)/2wd$, where the symbols indicated usual terms (see Table 1). By multiplying the flux J with S, we recover a clear trend, as shown in the $J \times S$ vs R plot in Fig. 3c. Interestingly, the shape of casting molds has also been shown to affect the metal solidification time, which however was not predicted by Chvorinov's rule [46].

3.4. Anomalous behaviour of nematic-columnar propagating front

Upon nucleation of the *N*-M interface close to the center of the microchannel, a distinct front travels on either direction, towards the channel ports. As reported in section 3.3, DMOAP treated nanoporous surfaces absorb water at a faster rate, yet the propagation speed of the nematic-columnar interface presents an opposite trend. Fig. 4a shows the *N*-M front position over time for the two anchoring conditions. The slope of the position vs time plot (inset) gives the front propagation speed, with a typical value of around 4 μm/min for plasma-treated confinements, and 2.5 μm/min–3 μm/min for the DMOAP-mediated front propagation. It is to be noted that the front speed decelerates over a distance: the deceleration rate is faster for the plasma-treated case than for the DMOAP-treated channel (Fig. 4a, inset). As the water molecules from the nematic phase of the DSCG solution confined within the ports (reservoirs) enter and dilute the relatively higher concentration of the DSCG solution within the channel, the effective PDMS surface area in contact with the nematic phase decreases, resulting in the deceleration of the *N*-M front speed. Intriguingly, the difference in the plasma- and DMOAP- mediated front speeds contradicts the trends in the water uptake rates reported in Fig. 3a, b. As the DMOAP-treated channel has been shown to uptake water faster (Fig. 3c), one expects the *N*-M front speed to be faster as well, since the rate of molecular transport should be proportional to the speed of the *N*-M (as reported in the single-component liquid–solid metal casting process [49,50]). These contrasting dynamics in the two-component water-DSCG systems is driven potentially by the emergence of high anisotropic elasticity at the phase transition. The higher the J, higher is the influx of water molecules from the nematic DSCG solution (in the ports) to the middle of the channels, thus resulting in further dilution and slowing of the *N*-M front. A similar case of dissolution of surfactant lamellar phase in a glass channel connected with water reservoir was presented by Capaccio *et al.* [51].

Once the M−phase nucleates, the propagating front gradually fills up the entire channel without leaving cracks or physical discontinuities. This is in contrast to our observations using isotropic crystal forming sodium chloride solution (Fig. 4b, c), indicating the potential role of elastic forces in driving the phase transitions. The saturated NaCl (30 % *w/v*) solution was clear when filled in the channel and after a few hours, as expected, the crystal nucleated at the centre. The crystals, however, didn't grow continuously as in case of DSCG, and left behind multiple cracks and local discontinuities. The clear contrasting differences in these two materials could be found in Fig. 4c. The time sequence captures the differences in the evaporative patterns of NaCl (top panel) vs DMOAP (lower panel): discrete NaCl crystals appear scattered as the drying droplet recedes over time due to evaporation. The DSCG on the other hand leaves a trail of tightly knitted grain structures as the evaporating drop recedes. We formulate a simple mathematical model to capture the dynamics of the front propagation in the microfluidic geometry (Fig. 4d, see Supplementary section for details of the 1-D model). Using a spring-mass system, we obtain a qualitative match with our experimental data (Fig. 4e), and demonstrate that the local front speed can be systematically tuned by varying the spring constant, k/m (a proxy for the emergent elastic interactions at the phase transition) in combination with the volume of the M−phase formed from a given volume of co-existing *N*-M phase (Ø).

3.5. Programming lyotropic phase transition via microfluidic geometry and topography

We leverage the spatial and temporal insights of the nematic to M−phase transition to demonstrate the programmability of lyotropic transition under isothermal conditions. As a first case, we consider *T*-shaped microchannels with variable arm lengths, offering simple but

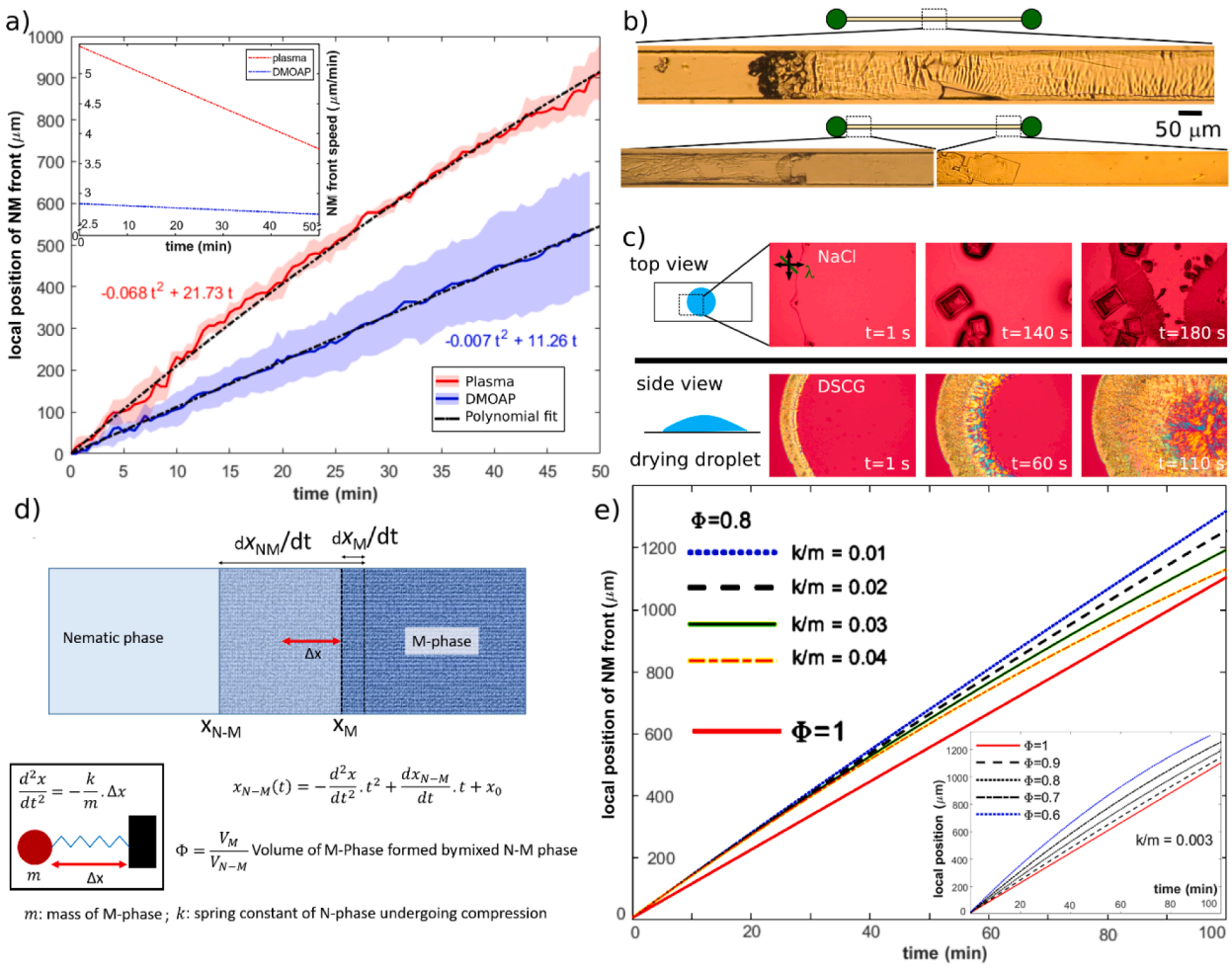

Fig. 4. (Colour figure) The nematic-M−phase interface in plasma-treated channels travel faster than that within DMOAP-treated channels. **(a)** Position of the *N*-M front over time for the 12 % DSCG-filled 200 × 15 μm channel for plasma (○) and DMOAP (□), obtained over 3 experimental replicates. Inset plots the front speeds over time for the corresponding cases. **(b)** Contrasting textures are observed when 30 % (w/v) NaCl is filled in 200 × 15 μm channel (top panel): the crystal formation occurs similarly at the centre of channel however the emerging textures is discontinuous. **(c)** Discontinuous domains emerge when 30 % (w/v) NaCl solution undergoes a phase transition (top row image sequence), in contrast to the 6 % DSCG solution drying on a plasma-treated glass slide, showing a continuous texture. The drying droplets are millimetric in dimension. **(d)** Schematic of the mathematical modelling framework, with the key parameters: spring constant, *k*, and *Ø*, the volume of compact M−phase emerging from the mixed *N*-M phase volume. Here, m is the mass of M−phase in the *N*-M−phase. **(e)** By varying the parameters *k* and *Ø* systematically, the general trend of the *N*-M front position was captured.

geometrically more complex confinement compared to the straight channels (Fig. 5a, b). In case of *T*-shaped channels with the horizontal arms longer than the vertical arm (Fig. 5a), the *N*-M phase transition initiates simultaneously in both the horizontal arms. The reservoirs at end of each arm drive the transition to M−phase first in the horizontal arms, which then converge towards the center, finally propagating towards the bottom arm (Fig. 5a). When we invert the geometrical condition, *i.e.,* the vertical arm is longer that the horizontal ones, the transition to M−phase initiated first within the vertical arm, followed by spreading across the rest of the *T*-shaped channel (Fig. 5b). We extend the programmable *N*-M phase transition concept to confinements of higher geometric complexity [13] such as the septapod, seven-armed channel in Fig. 5c. With one arm shorter than the rest, the *N*-M front nucleates first within the longer arms (arms b–g in Fig. 5c), and propagates away from the ports to finally converge at the septapod junction. Thereafter the *N*-M front can continue travelling to the shorter arm (arm-a), before filling up the shorter microfluidic arm (arm-a).

In addition to channel geometry, we alter the embedded topography by incorporating micro-pillars within the microfluidic devices (Fig. 5d, and e). A micropillar, due to its nanoporous surface, can enhance the local water uptake rate, thereby driving the system to an *N*-M phase transition faster. Fig. 5d presents a square-shaped cylindrical PDMS pillar placed in the middle of a straight channel, which has induced the *N*-M phase transition locally. Such pillars could be offset from the central position, thereby shifting the location and rapidity of the M−phase formation. These results enable flexible lyotropic phase-transition concepts mediated by the confinement geometry and internal topography of the channel surfaces. Finally, by introducing micron sized tracer particles in the channel, we reveal the emergence of elasto-advective flows during the nematic-M−phase transition (Fig. 5f). Particles dispersed in the lyotropic LC phase get pulled toward the less mobile M−Phase, opposite to the direction of the travelling *N*-M front. The inherent elastic nature of LCLC does not allow the M−phase to be discontinuous (unlike in NaCl solution), resulting in stored elastic energy which can be released by infusing water molecules into the system. With *et al.* have utilized multiple arm microfluidic channels with controlled flow rates to spatially induce lyotropic phase transition [52]. Similarly, other biopolymers like DNA, and pectin have been made to produce compact aggregates, spatially at a desired location in the microfluidic channels, utilizing the precise control of flow properties and diffusion of these molecules along the channels [53,54]. Our results, in contrast to the previous reports, do not employ any external driving mechanisms like

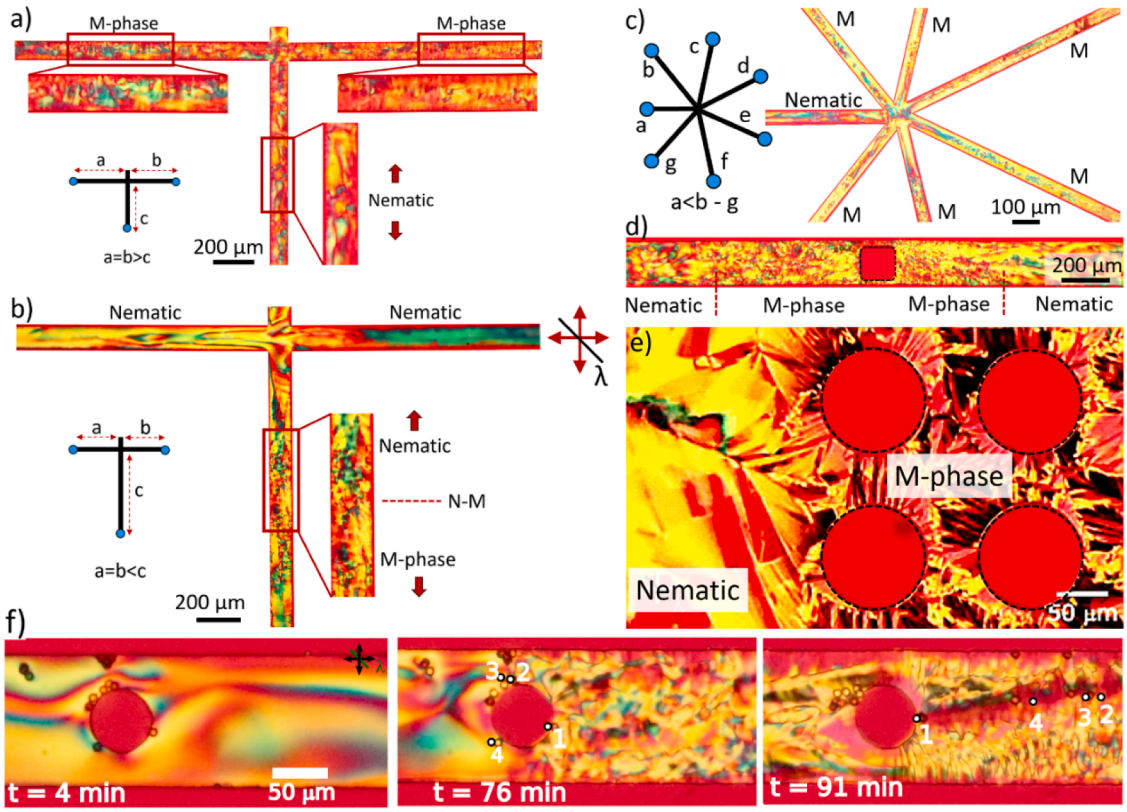

Fig. 5. (Colour figure) Spatio-temporal programming of isothermal phase transition in nanoporous microchannels. **(a)** *T*-junction channel with 3 arms connected to the ports. By varying the length of one arm, relative to the other two arms, the *N*-M phase transition nucleation point could be offset. The longer arms (arms a and b) of the *T*-channel yield M−phase, whereas the shorter arm (arm-c) maintains nematic phase. **(b)** Now by changing the relative arm lengths, *N*-M phase transition could be triggered in the longer c-arm, while other two arms retained the nematic phase. **(c)** The concept was extended to multi-arm channels, shown here for a septapod where the shortest arm (arm-a) retains the nematic phase. **(d)** Insertion of topographical features can induce local *N*-M phase transition: close to the square pillar (marked with dotted black lines) M−phase is observed, while far away from the pillar, nematic phase is recorded. **(e)** M−phase localization using a pillar network: Pillar-dense regions undergo phase transition from nematic to M−phase, while pillar-sparse regions retain nematic phase. **(f)** Elasto-advective transport of ~5 µm particles due to emergent long-range order during the *N*-M transition offers novel spatio-temporal particle manipulation concepts. Typical particle transport rate is 2.1 ± 0.3 µm/min.

pump-driven flows, and instead is uniquely dependent on the uptake of water by the nanoporous PDMS walls. The high degree of spatio-temporal control – enabled by the geometry, anchoring, wettability and topography – pave the way for producing self-assembled complex functional materials [55]. Going beyond applications of lyotropic phase transition in a range of stimuli-responsive materials relevant for drug delivery and wound healing [56–61], our results offer a physical and programmable route to biologically-relevant phase transitions in lyotropic systems [62,63], evoking a fresh take on surface-mediated molecular self-assembly under generic nanoporous settings, with potential ramifications in our understanding of the prebiotic world [31].

4. Conclusions

By using DSCG as a model lyotropic liquid crystal we have demonstrated that the intrinsic PDMS nanoporosity and confinement cross-section, together with the imposed wettability regulate the rate of the nematic-M−phase transition. We have mapped out the contributions of surface anchoring conditions, geometric factors, and design of nanoporous microfluidic channel on nematic-M phase transition while illustrating the emergent elasticity that arises along. Selective permeation of water through nanoporous PDMS-based rectangular microchannel resembles heat diffusion during metal casting. Hence, our results show the grain structures of M−phase of DSCG analogous to those of solidified metal during casting. The kinetics of phase transition from nematic (N) to M−phase (M) was shown to be influenced by the surface-to-volume ratio, shape factor and surface wettability, which in turn affects the kinetics of water uptake. The hydrophilic plasma treated surface of PDMS hindered the water uptake rate compared to hydrophobic DMOAP treated surface. Our results provide a mechanistic understanding of the kinetics of LCLC phase transition in PDMS-glass microfluidic devices, and highlight the role of the surface anchoring conditions and confinement dimensions as key determinants of the phase transition process (at a given temperature). By introducing particles in the channel along with DSCG, we could observe elasto-advective transport arising during N to M phase transition that, owing to the reversibility of the *N*-M phase transition process (see Supplementary figure S5), could be exploited for designing micro-actuators [64]. This together with the rich landscape of LCLC behaviour on patterned surfaces [65], the spontaneous emergent properties [66], and the general anisotropy-mediated flow characteristics of LCs in microscales [67,68] can offer interesting routes to next generation of fluid-particle manipulation and guidance concepts.

Funding

This work is supported by the ATTRACT Investigator Grant (to A.S., Grant no. A17/MS/11572821/MBRACE) and CORE Grant (C19/MS/13719464/TOPOFLUME/Sengupta) of the Luxembourg National Research Fund; and donations from the CINVEN Foundation.

Author Contributions

A.S. conceptualized and developed the research plan, and directed all parts of the project. V.U. carried out experiments, analyzed the data and developed the mathematical model with inputs from A.S. V.U. and A.S. prepared the figures and wrote the paper.

CRediT authorship contribution statement

Vamseekrishna Ulaganathan: Investigation, Methodology, Writing – original draft, Writing – review & editing, Visualization. **Anupam Sengupta:** Conceptualization, Methodology, Validation, Investigation, Resources, Writing – original draft, Writing – review & editing, Visualization, Supervision, Project administration, Funding acquisition.

Declaration of Competing Interest

The authors declare that they have no known competing financial interests or personal relationships that could have appeared to influence the work reported in this paper.

Data availability

All data and codes are available in the main text and the Supplementary materials, or can be obtained upon requests made to the corresponding author.

Acknowledgements

The authors thank Anshul Sharma, Sharadhi Nagaraja, Marco G. Mazza and Jayabrata Dhar for valuable discussions during the course of this work.

Appendix A. Supplementary materials

Supplementary data to this article can be found online at https://doi.org/10.1016/j.jcis.2023.06.010.

References

[1] P. Tabeling, Introduction to Microfluidics, Oxford University Press, 2011.
[2] P. Kim, et al., Soft lithography for microfluidics: a review, Biochip J. 2 (2008) 1–11.
[3] M.K. Raj, S. Chakraborty, Fluid Dynamics in Deformable Microchannels, Springer Mechanical Sciences, Singapore, 2021, pp. 145–167.
[4] K.C. Bhargava, B. Thompson, N. Malmstadt, Discrete elements for 3D microfluidics, Proc. Nat. Acad. Sci. 111 (2014) 15013–15018.
[5] G.D. Chen, F. Fachin, M. Fernandez-Suarez, B.L. Wardle, M. Toner, Nanoporous elements in microfluidics for multiscale manipulation of bioparticles, Small 7 (2011) 1061–1067.
[6] V. Drebezghova, H. Gojzewski, A. Allal, M.A. Hempenius, C. Nardin, G.J. Vancso, Network mesh nanostructures in cross-linked poly (dimethylsiloxane) visualized by AFM, Macromol. Chem. Phys. 221 (2020) 2000170.
[7] K. Efimenko, W.E. Wallace, J. Genzer, Surface modification of Sylgard-184 poly (dimethyl siloxane) networks by ultraviolet and ultraviolet/ozone treatment, J. Colloid Interface Sci. 254 (2002) 306–315.
[8] D. Bodas, C. Khan-Malek, Hydrophilization and hydrophobic recovery of PDMS by oxygen plasma and chemical treatment—An SEM investigation, Sens. Actuators B 123 (2007) 368–373.
[9] A. Sengupta, B. Schulz, E. Ouskova, C. Bahr, Functionalization of microfluidic devices for investigation of liquid crystal flows, Microfluid. Nanofluid. 13 (2012) 941–955.
[10] H. Hillborg, et al., Crosslinked polydimethylsiloxane exposed to oxygen plasma studied by neutron reflectometry and other surface specific techniques, Polymer 41 (2000) 6851–6863.
[11] A. Sengupta, Topological constraints in a microfluidic platform, Liq. Cryst. 41 (2014) 290–301.
[12] A. Sengupta, S. Herminghaus, C. Bahr, Liquid crystal microfluidics: surface, elastic and viscous interactions at microscales, Liq. Cryst. Rev. 2 (2014) 73–110.
[13] L. Giomi, Ž. Kos, M. Ravnik, A. Sengupta, Cross-talk between topological defects in different fields revealed by nematic microfluidics, Proc. Natl. Acad. Sci. 114 (2017) E5771–E5777.
[14] J. Uchida, et al., Advanced functional liquid crystals, Adv. Mater. 34 (2022) 2109063.
[15] J. Quintans Carou, B.R. Duffy, N.J. Mottram, S.K. Wilson, Shear-driven and pressure-driven flow of a nematic liquid crystal in a slowly varying channel, Phys. Fluids 18 (2006), 027105.
[16] T. Emeršič, R. Zhang, Ž. Kos, S. Čopar, N. Osterman, J.J. De Pablo, U. Tkalec, Sculpting stable structures in pure liquids, Sci. Adv. 5 (2019) eaav4283.
[17] Ž. Kos, M. Ravnik, Field generated nematic microflows via backflow mechanism, Sci. Rep. 10 (2020) 1–10.
[18] K. Fedorowicz, R. Prosser, On the flow of liquid crystals through 90° bends, Phys. Fluids 34 (2022), 063106.
[19] M. Lesniewska, N. Mottram, O. Henrich, Controllable particle migration in liquid crystal flows, Soft Matter. (2022), https://doi.org/10.1039/D2SM00707J.
[20] A. Sengupta, C. Bahr, S. Herminghaus, Topological microfluidics for flexible micro-cargo concepts, Soft Matter. 9 (2013) 7251–7260.
[21] A. Sengupta, U. Tkalec, M. Ravnik, J.M. Yeomans, C. Bahr, S. Herminghaus, Liquid crystal microfluidics for tunable flow shaping, Phys. Rev. Lett. 110 (2013), 048303.
[22] A. Sengupta, Tuning Fluidic Resistance via Liquid Crystal Microfluidics, Int. J. Mol. Sci. 14 (2013) 22826–22844.
[23] A. Sengupta, Topological microfluidics: present and prospects, Liquid Crystals Today 24 (2015) 70–80.
[24] I. Dierking, A. Martins Figueiredo Neto, Novel trends in lyotropic liquid crystals, Crystals 10 (2020) 604.
[25] X. Yao, et al., Orientational order of a lyotropic chromonic liquid crystal measured by polarized Raman spectroscopy, J. Phys. Chem. B 120 (2016) 4508–4512.
[26] J.E. Lydon, Chromonic liquid crystal phases, Curr. Opin. Colloid Interface Sci. 3 (1998) 458–466.
[27] D.M. Agra-Kooijman, G. Singh, A. Lorenz, P.J. Collings, H.S. Kitzerow, S. Kumar, Columnar molecular aggregation in the aqueous solutions of disodium cromoglycate, Phys. Rev. E 89 (2014), 062504.
[28] S. Zhou, Elasticity, viscosity, and orientational fluctuations of a lyotropic chromonic nematic liquid crystal disodium cromoglycate, in: Lyotropic Chromonic Liquid Crystals, Springer, Cham, 2017, pp. 51–75.
[29] Zhang, Q., Zhang, R., Ge, B., Yaqoob, Z., So, P. T., & Bischofberger, I., Structures and topological defects in pressure-driven lyotropic chromonic liquid crystals, in: Proceedings of the National Academy of Sciences 118, 2021, e2108361118.
[30] A. Sharma, I.L.H. Ong, A. Sengupta, Time dependent lyotropic chromonic textures in microfluidic confinements, Crystals 11 (2021) 35.
[31] G.F. Joyce, The antiquity of RNA-based evolution, Nature 418 (2002) 214–221.
[32] S.M. Hong, et al., Hydrophilic surface modification of PDMS using atmospheric RF plasma, J. Phys.: Conf. Series 34 (2006).
[33] R.G. Laughlin, Surfactant phase science, Curr. Opin. Colloid Interface Sci. 1 (1996) 384–390.
[34] J.A. Stewart, et al., The phase behaviour of lyotropic liquid crystals in linear alkylbenzene sulphonate (LAS) systems, Colloids Surf. A Physicochem. Eng. Asp. 338 (2009) 155–161.
[35] P. Kékicheff, Phase diagram of sodium dodecyl sulfate-water system: 2. Complementary isoplethal and isothermal phase studies, J. Colloid Interface Sci. 131 (1989) 133–152.
[36] G.C. Randall, P.S. Doyle, Permeation-driven flow in poly (dimethylsiloxane) microfluidic devices, Proc. Nat. Acad. Sci. 102 (2005) 10813–10818.
[37] G.A. Ferreira, Geometric features in lyotropic liquid crystalline phase transitions observed in aqueous surfactant systems, J. Dispers. Sci. Technol. 1–14 (2021).
[38] G. Straffelini, L. Lutterotti, M. Tonolli, M. Lestani, Modeling solidification microstructures of steel round billets obtained by continuous casting, ISIJ Int. 51 (2011) 1448–1453.
[39] M. El-Bealy, B.G. Thomas, Prediction of dendrite arm spacing for low alloy steel casting processes, Metall. Mater. Trans. B 27 (1996) 689–693.
[40] S. Gowri, F.H. Samuel, Effect of cooling rate on the solidification, Metall. Trans. A 23 (1992) 3369–3376.
[41] J.W. Fu, Y.S. Yang, J.J. Guo, W.H. Tong, Effect of cooling rate on solidification microstructures in AISI 304 stainless steel, Mater. Sci. Technol. 24 (2008) 941–944.
[42] M.P. Groover, Fundamentals of modern manufacturing: materials, processes, and systems, John Wiley & Sons, 2020.
[43] Y. Hendrikx, B. Pansu, Sequence of phase transformations in the ternary lyotropic system sodium decyl sulfate/2-octanol/water, J. Phys. II (6) (1996) 33–47.
[44] I. Martiel, et al., Facile dispersion and control of internal structure in lyotropic liquid crystalline particles by auxiliary solvent evaporation, Langmuir 30 (2014) 14452–14459.
[45] E.Y. Topuzlu, et al., Role of water in the lyotropic liquid crystalline mesophase of lithium salts and non-ionic surfactants, Langmuir 37 (2021) 14443–14453.
[46] H. Modaressi, G. Garnier, Mechanism of wetting and absorption of water droplets on sized paper: Effects of chemical and physical heterogeneity, Langmuir 18 (2002) 642–649.
[47] Riaz, A. *et al.,* Thin film diffusion barrier formation in PDMS microcavities, in: *Transducers 2009-2009 International Solid-State Sensors, Actuators and Microsystems Conference. IEEE*, 2009, pp. 1051–1054.
[48] M. Ahmadlouydarab, J.J. Feng, Motion and coalescence of sessile drops driven by substrate wetting gradient and external flow, J. Fluid Mech. 746 (2014) 214–235.
[49] M. Tiryakioğlu, E. Tiryakioğlu, D.R. Askeland, The effect of casting shape and size on solidification time: a new approach, Int. J. Cast Met. Res. 9 (1997) 259–267.
[50] C. Stolze, T. Janoschka, U.S. Schubert, F.A. Müller, S. Flauder, Directional solidification with constant ice front velocity in the ice-templating process, Adv. Eng. Mater. 18 (2016) 111–120.
[51] A. Capaccio, et al., Dissolution of a surfactant-water lamellar phase investigated by combining time-lapse polarized light microscopy and confocal Raman spectroscopy, J. Colloid Interface Sci. 561 (2020) 136–146.

[52] S. With, et al., Fast diffusion-limited lyotropic phase transitions studied in situ using continuous flow microfluidics/microfocus-SAXS, Langmuir 30 (2014) 12494–12502.
[53] C. Iliescu, G. Tresset, Microfluidics-driven strategy for size-controlled DNA compaction by slow diffusion through water stream, Chem. Mater. 27 (2015) 8193–8197.
[54] M. Marquis, J. Davy, A. Fang, D. Renard, Microfluidics-assisted diffusion self-assembly: Toward the control of the shape and size of pectin hydrogel microparticles, Biomacromolecules 15 (2014) 1568–1578.
[55] R. Mezzenga, et al., Nature-inspired design and application of lipidic lyotropic liquid crystals, Adv. Mater. 31 (2019) 1900818.
[56] Y. Huang, S. Gui, Factors affecting the structure of lyotropic liquid crystals and the correlation between structure and drug diffusion, RSC Adv. 8 (2018) 6978–6987.
[57] C. Wang, et al., Improving water-absorption and mechanical strength: lyotropic liquid crystalline-based spray dressings as a candidate wound management system, AAPS Pharm. Sci. Tech. 23 (2022) 1–10.
[58] X. Zhang, et al., Smart phase transformation system based on lyotropic liquid crystalline hard capsules for sustained release of hydrophilic and hydrophobic drugs, Drug Deliv. 27 (2020) 449–459.
[59] H. Zhang, Z. Wang, Phase transition and release kinetics of polyphenols encapsulated lyotropic liquid crystals, Int. J. Pharm. 565 (2019) 283–293.
[60] J. Fan, H. Zhang, M. Yi, F. Liu, Z. Wang, Temperature induced phase transformation and in vitro release kinetic study of dihydromyricetin-encapsulated lyotropic liquid crystal, J. Mol. Liq. 274 (2019) 690–698.
[61] X. Yue, et al., A bacteria-resistant and self-healing spray dressing based on lyotropic liquid crystals to treat infected post-operative wounds, J. Mater. Chem. B 9 (2021) 8121–8137.
[62] Neto, Antônio M. Figueiredo, and Silvio RA Salinas. The physics of lyotropic liquid crystals: Phase transitions and structural properties. Vol. 62, OUP Oxford, 2005.
[63] Y. Huang, S. Gui, Factors affecting the structure of lyotropic liquid crystals and the correlation between structure and drug diffusion, RSC Adv. 8 (13) (2018) 6978–6987.
[64] M. Mazurek-Budzyńska, et al., 4D-actuators by 3D-printing combined with water-based curing, Mater. Today Commun. 30 (2022), 102966.
[65] J.-Y. Kim, et al., Macroscopic alignment of chromonic liquid crystals using patterned substrates, Phys. Chem. Chem. Phys. 18 (2016) 10362–10366.
[66] Nayani, et al., Spontaneous emergence of chirality in achiral lyotropic chromonic liquid crystals confined to cylinders, Nat. Commun. 6 (2015) 8067.
[67] A. Sengupta, Topological microfluidics: Nematic liquid crystals and nematic colloids in microfluidic environment, Springer International Publishing, Cham, Switzerland, 2013.
[68] P. Steffen, E. Stellamanns, A. Sengupta, Surface anchoring mediates bifurcation in nematic microflows within cylindrical capillaries, Phys. Fluids 33 (2021), 072005.